Analysis and optimization of weakly coupled thermoelastoplastic systems with applications to Weldment design

ARTICLE *in* INTERNATIONAL JOURNAL FOR NUMERICAL METHODS IN ENGINEERING · APRIL 1995

Impact Factor: 2.06 · DOI: 10.1002/nme.1620380803

3 AUTHORS, INCLUDING:

Creto Vidal
Universidade Federal do Ceará

71 PUBLICATIONS **400** CITATIONS

SEE PROFILE

INTERNATIONAL JOURNAL FOR NUMERICAL METHODS IN ENGINEERING, VOL. 38, 1259–1285 (1995)

ANALYSIS AND OPTIMIZATION OF WEAKLY COUPLED THERMOELASTOPLASTIC SYSTEMS WITH APPLICATIONS TO WELDMENT DESIGN

PANAGIOTIS MICHALERIS

Edison Welding Institute, Columbus, OH, U.S.A

DANIEL A. TORTORELLI

Department of Mechanical and Industrial Engineering and Department of Theoretical and Applied Mechanics, University of Illinois of Champaign, Urbana, IL, U.S.A.

CRETO A. VIDAL

Departamento de Computacao Universidade Federal do Ceara', Fortaleza, Ceara', Brazil.

SUMMARY

A systematic approach for the design of weakly coupled thermoelastoplastic systems is presented. The Newton–Raphson iteration method is used in the solution process so that analytic design sensitivity formulations may be efficiently derived via the direct differentiation technique. The derived formulations are suitable for finite element implementations. Analysis and sensitivity analysis capabilities are combined with numerical optimization to form an optimum design algorithm. To demonstrate the algorithm, we optimally design a weldment with respect to manufacturing and service life aspects.

KEY WORDS: sensitivity analysis; optimization, FEM; thermoelastoplasticity; welding

1. INTRODUCTION

1.1. Optimization of weakly coupled thermoelastoplastic systems

Engineering design is an iterative process, in which a design is continuously modified until it satisfies the design goals. The increasing complexity of today's engineering designs renders the traditional 'trial-and-error' design process, based on experience and intuition, insufficient and necessitates the utilization of more systematic methods such as design sensitivity analysis and numerical optimization.

Design sensitivity analysis and numerical optimization are successfully used to design minimum weight structures with linear behaviour.[1–3] In the present work, this approach is used to optimize systems governed by the non-linear equations of thermoelastoplastic systems. In the optimization problem, an initial design comprised of the shape, boundary conditions, loading and material properties, is parametrized by a set of design parameters. Generalized response functionals are then defined to quantify cost and constraint specifications. These response functionals depend on the design parameters both explicitly and implicitly through the system response, which is evaluated in the analysis, e.g. temperature, heat flux, displacement, stress, strain and reaction forces. The, optimization iterations commence when the analysis is performed and the

CCC 0029–5981/95/081259–27

Received 18 November 1993
Revised 25 April 1994

computed response is used to evaluate cost and constraint functionals. An analytic sensitivity analysis is then performed to evaluate the derivatives of the cost and constraint functionals with respect to the design parameters. The numerical optimization program uses the values of the cost and constraint functionals and their sensitivities to modify the design parameter values to minimize the cost functional and satisfy the constraints. Convergence criteria are evaluated to determine if more iterations are required.

Sensitivity analysis for linear structural systems is a well-established field—see References 4 and 5. Sensitivity formulations for non-linear elastic systems have also been studied in References 6–16 and for elastoplastic systems in References 17–24. Additional works formulate sensitivities for thermal systems—see References 25–34. Sensitivities for coupled thermoelastic systems are derived in References 35–37 and sensitivities for coupled non-linear thermoelastic systems are investigated in References 38–40. The development of analytic sensitivity analyses of coupled thermoelastoplastic systems is an area of ongoing research.

In this paper, the analysis and sensitivity analysis for weakly coupled thermoelastoplastic systems are derived. The tangent operators of the Newton–Raphson solution processes are used to compute sensitivities accurately and efficiently via the direct differentiation method. The thermal analysis and sensitivity analysis are consistent with those presented in References 32 and 33. The elastoplastic analysis and sensitivity analysis follow the formulation presented in Reference 16 for transient non-linear coupled systems. The analysis and sensitivity analysis are incorporated into a numerical optimization algorithm to design a weldment.

1.2. Weldment stress analysis and optimization

Residual stress development in weldments received considerable attention during the 1950s and 1960s using experimental and analytical methods (cf. References 41 and 42). Numerical methods were used first to predict residual stress and distortion during the 1970s—see References 43–47. More recently, thermal analyses have been performed in References 48–52. In other welding processing analyses, Argyris *et al.*[48] performed a two-dimensional thermoviscoplastic finite element analysis. Elastoplastic finite element analyses are performed to predict residual stress in References 53 and 54 and solid state phase transformations are considered in References 44,48 and 55–57. Design sensitivity analysis and numerical optimization is applied to design weldments in Reference 58; however, only linear thermoelastic behaviour is considered.

In this work, the residual stresses which evolve during the welding process are predicted by solving a non-linear transient thermoelastoplastic problem. The sensitivities of the thermal and mechanical fields are then efficiently computed via the direct differentiation method. Finally, the analysis and sensitivity analysis results are used to optimize a weldment design.

2. WEAKLY COUPLED THERMOPLASTIC SYSTEMS

In this section, the analysis and the corresponding sensitivity analysis for weakly coupled thermoplastic systems are derived. These systems are only weakly coupled because the mechanical work is neglected in the energy equation.

2.1. Primal analysis

First, the primal analysis, i.e. the evaluation of thermal and mechanical response fields, is discussed. The energy and momentum balance equations and the mechanical constitutive laws are expressed in residual form and solved iteratively by the Newton–Raphson method. The

transient thermal analysis preceds the quasi-static elastoplastic mechanical analysis since the problem is treated as weakly coupled. A numerical solution is obtained by discretizing the time domain and evaluating the time integrals with the inherently stable backward Euler integration scheme. However, other integration schemes may also be incorporated (e.g. forward Euler[48] or the variable midpoint algorithm[23]).

2.1.1. Thermal analysis. The finite element formulation for thermal systems is presented in References 32 and 59 and is briefly discussed here for completeness.

The initial-boundary value problem is defined over the spatial domain V with boundary A. The boundary is comprised of two complementary subsurfaces A_T and A_q, over which prescribed temperature and surface flux boundary conditions are, respectively, applied. The time domain $[0, {}^{M}t]$ is divided into M intervals.

The energy balance equation at time* ${}^{n}t$, after time discretization, is written as

$$\frac{\partial {}^{n}h}{\partial T}\frac{{}^{n}T - {}^{n-1}T}{{}^{n}t - {}^{n-1}t} = -\nabla \cdot {}^{n}\mathbf{q} + {}^{n}r \quad \text{in } V \tag{1}$$

where T is the temperature, h is the enthalpy per unit volume, $\mathbf{q}$ is the heat flux vector, r is the internal heat generation and ∇ is the spatial gradient operator.

The non-linear isotropic Fourier heat flux constitutive relation is enforced:

$${}^{n}\mathbf{q} = -{}^{n}k\nabla {}^{n}T \tag{2}$$

where k is the temperature-dependent thermal conductivity.

The initial temperature field is defined as

$${}^{0}T = T^{0} \quad \text{on } V \tag{3}$$

where T^0 is the prescribed initial temperature, and the following boundary conditions are applied:

$${}^{n}T = {}^{n}T^{P} \quad \text{on } A_T \tag{4}$$

$${}^{n}q^{s} = {}^{n}q^{P} \quad \text{on } A_q \tag{5}$$

where T^P and q^P represent the prescribed temperature and temperature-dependent surface flux, respectively. The surface flux q^s is evaluated from

$${}^{n}q^{s} = {}^{n}\mathbf{q} \cdot \mathbf{n} \quad \text{on } A \tag{6}$$

where $\mathbf{n}$ is the unit outward normal to the surface A.

Integration by parts and application of the divergence theorem yields the usual variational form of the initial-boundary value problem,

$$\int_V \left\{ \nabla \hat{T} \cdot {}^{n}\mathbf{q} + \hat{T}\left[{}^{n}r - \frac{\partial {}^{n}h}{\partial T}\frac{{}^{n}T - {}^{n-1}T}{{}^{n}t - {}^{n-1}t} \right] \right\} \mathrm{d}V - \int_{A_q} \hat{T}\, {}^{n}q^{P}\, \mathrm{d}A = 0 \tag{7}$$

where $\hat{T}$ is any kinematically admissible function and equations (2)–(6) are strictly enforced.

In the finite element analysis of the initial-boundary value problem of equations (2)–(4), and (6) and (7), the spatial domain V is subdivided into piecewise regular subregions, i.e. elements. Then, a global residual vector $\mathscr{R}$ is formed from equation (7) by assembling the element residual

* Left superscripts denote the time at which the quantity is evaluated, i.e. ${}^{n}f = f|_{{}^{n}t}$

contributions which are evaluated by Gaussian quadratures[60] i.e.,

$$ {}^{n}\mathscr{W}({}^{n}\mathscr{T}, {}^{n-1}\mathscr{T}) \equiv \sum_{\text{elements}} \left\{ \sum_{\text{Gauss points}} {}^{n}\mathbf{W}({}^{n}T, {}^{n-1}T) \right\} = \mathbf{0} \tag{8} $$

where $\mathscr{T}$ is the global nodal temperature vector. The Gauss point residual $\mathbf{W}$ is computed from

$$ {}^{n}\mathbf{W}({}^{n}T, {}^{n-1}T) = \mathbf{B}^{\mathrm{T}}\,{}^{n}\mathbf{q} w J + \mathbf{N}^{\mathrm{T}} \left[{}^{n}r - \frac{\partial^{n} h}{\partial T} \frac{{}^{n}T - {}^{n-1}T}{{}^{n}t - {}^{n-1}t} \right] w J - \mathbf{N}^{\mathrm{T}n} q^{P} w j \tag{9} $$

where $\mathbf{N}$ and $\mathbf{B}$ are the usual matrices, which when combined with the element nodal temperature vector $\mathbf{T}$, interpolate the element temperature T, and temperature gradient ∇T, respectively. Finally, J and j are the volume and area metrics and w is the Gaussian weighting function.

The Newton–Raphson iterative process is utilized for the solution of equation (8). For a time step n, the incremental nodal temperature vector $\delta\mathscr{T}$, for a current solution estimate ${}^{n}T^{I}$, is determined by linearizing equation (8), i.e.

$$ \sum_{\text{elements}} \left\{ \sum_{\text{Gauss points}} \frac{\partial^{n}\mathbf{W}}{\partial^{n}T}\bigg|_{{}^{n}T^{I}} \right\} \delta\mathscr{T} = - \sum_{\text{elements}} \left\{ \sum_{\text{Gauss points}} {}^{n}\mathbf{W}\bigg|_{{}^{n}T^{I}} \right\} \tag{10} $$

where $\cdot|_{{}^{n}T^{I}}$ denotes that a quantity is evaluated at the current solution estimate ${}^{n}T^{I}$. The left-hand-side operator of equation (10) is deemed the tangent operator. Once $\delta\mathscr{T}$ is evaluated, the global nodal temperature vector ${}^{n}\mathscr{T}$ is updated from the sum

$$ {}^{n}\mathscr{T}^{I+1} = {}^{n}\mathscr{T}^{I} + \delta\mathscr{T} \tag{11} $$

The Newton–Raphson iterations eventually converge* to the solution ${}^{n}\mathscr{T}$, after which the time is incremented and the process is repeated.

2.1.2. Mechanical analysis. For the mechanical analysis, the boundary A is subdivided into two additional complementary subsurfaces $A_{\mathbf{u}}$ and $A_{\mathbf{t}}$, with prescribed displacement and traction, respectively. Again, the time domain is discretized† into M intervals and the backward Euler time integration scheme is incorporated. Quasi-static loading is assumed so the inertia effects are neglected.

Equilibrium at each time step n gives

$$ \nabla\cdot{}^{n}\boldsymbol{\tau} + {}^{n}\mathbf{b} = \mathbf{0} \quad \text{in } V \tag{12} $$

where $\boldsymbol{\tau}$ and $\mathbf{b}$ are the stress tensor and body force fields, respectively.

Infinitesimal deformations are assumed so that the strain–displacement relation reduces to

$$ {}^{n}\boldsymbol{\varepsilon}({}^{n}\mathbf{u}) = \tfrac{1}{2}[\nabla\,{}^{n}\mathbf{u} + (\nabla\,{}^{n}\mathbf{u})^{\mathrm{T}}] \tag{13} $$

where $\mathbf{u}$ is the displacement vector field. Furthermore, the total strain tensor $\boldsymbol{\varepsilon}$ is expressed as a sum of its elastic part $\boldsymbol{\varepsilon}_{\mathrm{E}}$ and plastic part $\boldsymbol{\varepsilon}_{\mathrm{p}}$:

$$ {}^{n}\boldsymbol{\varepsilon} = {}^{n}\boldsymbol{\varepsilon}_{\mathrm{E}} + {}^{n}\boldsymbol{\varepsilon}_{\mathrm{p}} \tag{14} $$

---

* Note that existence and uniqueness of the solution to nonlinear problems is not necessarily guaranteed. Hence, the problem may not converge

† The time discretization for the mechanical analysis is, in general, independent of the time discretization of the thermal analysis. If the discretization of the thermal and mechanical analyses differ, interpolation is required

The constitutive relations consist of the plastic strain and internal variable evolution laws and the stress–strain relation, which are shown here in discrete form,† i.e.

$$ {}^{n}\boldsymbol{\varepsilon}_{\mathrm{p}} = {}^{n-1}\boldsymbol{\varepsilon}_{\mathrm{p}} + ({}^{n}\lambda - {}^{n-1}\lambda)\,\mathbf{f}({}^{n}\boldsymbol{\tau}, {}^{n}\mathbf{p}, {}^{n}T) \quad \text{in } V \tag{15} $$

$$ {}^{n}\mathbf{p} = {}^{n-1}\mathbf{p} + ({}^{n}\lambda - {}^{n-1}\lambda)\,\mathbf{h}({}^{n}\boldsymbol{\tau}, {}^{n}\mathbf{p}, {}^{n}T) \quad \text{in } V \tag{16} $$

$$ {}^{n}\boldsymbol{\tau} = {}^{n-1}\boldsymbol{\tau} + \mathbf{C}({}^{n}T)[\boldsymbol{\varepsilon}({}^{n}\mathbf{u}) - \boldsymbol{\varepsilon}({}^{n-1}\mathbf{u}) - {}^{n}\boldsymbol{\varepsilon}_{\mathrm{p}} + {}^{n-1}\boldsymbol{\varepsilon}_{\mathrm{p}} - \alpha({}^{n}T)({}^{n}T - {}^{n-1}T)\mathbf{I}_{\tau}] \quad \text{in } V \tag{17} $$

where λ is the plastic multiplier, $\mathbf{f}$ is the plastic flow vector, $\mathbf{p}$ is the m-dimensional internal variable vector whose components describe internal dissipation mechanisms and $\mathbf{h}$ is the hardening relation vector that governs the evolution of $\mathbf{p}$. Additionally, $\mathbf{C}$ is the elastic constitutive tensor and α is the differential thermal expansion coefficient; both quantities are temperature dependent. Finally, $\mathbf{I}_{\tau}$ is the identity operator in the stress space (cf. Reference 61).

The Kuhn–Tucker complementary conditions determine whether elastic behaviour, loading, neutral loading or unloading occurs, and are given in discrete form by

$$ 0 \leqslant {}^{n}\lambda - {}^{n-1}\lambda \quad \text{in } V \tag{18} $$

$$ 0 \geqslant Y({}^{n}\boldsymbol{\tau}, {}^{n}\mathbf{p}, {}^{n}T) \quad \text{in } V \tag{19} $$

$$ 0 = ({}^{n}\lambda - {}^{n-1}\lambda)\,Y({}^{n}\boldsymbol{\tau}, {}^{n}\mathbf{p}, {}^{n}T) \quad \text{in } V \tag{20} $$

where Y is the yield function. For a detailed presentation of the plasticity theory see References 62–64.

The boundary conditions are

$$ {}^{n}\mathbf{u} = {}^{n}\mathbf{u}^{P} \quad \text{on } A_{\mathrm{u}} \tag{21} $$

$$ {}^{n}\mathbf{t} = {}^{n}\mathbf{t}^{P} \quad \text{on } A_{\mathrm{t}} \tag{22} $$

where $\mathbf{t}$ is the traction vector which is related to the stress tensor $\boldsymbol{\tau}$ through the Cauchy relation

$$ {}^{n}\mathbf{t} = {}^{n}\boldsymbol{\tau}\cdot\mathbf{n} \quad \text{on } A \tag{23} $$

Application of the principle of virtual work yields the following variational form for the boundary value problem:

$$ \int_{V} \boldsymbol{\varepsilon}(\hat{\mathbf{u}})\,{}^{n}\boldsymbol{\tau}\,\mathrm{d}V - \int_{V} \hat{\mathbf{u}}\,{}^{n}\mathbf{b}\,\mathrm{d}V - \int_{A_{\mathrm{t}}} \hat{\mathbf{u}}\,{}^{n}\mathbf{t}^{P}\,\mathrm{d}V = 0 \tag{24} $$

where $\hat{\mathbf{u}}$ is any kinematically admissible displacement field and equations (13)–(23) are strictly enforced.

Finite element discretization of equation (24) is used to form the residual $\mathscr{R}$ in a manner analogous to equation (8), i.e.

$$ {}^{n}\mathscr{R}({}^{n}\mathscr{U}, {}^{n-1}\mathscr{U}, {}^{n}\mathscr{V}, {}^{n-1}\mathscr{V}, {}^{n}\mathscr{T}, {}^{n-1}\mathscr{T}) \equiv \sum_{\text{elements}} \left\{ \sum_{\text{Gauss points}} {}^{n}\mathbf{R} \right\} = \mathbf{0} \tag{25} $$

where $\mathscr{U}$ is the global nodal displacement vector. The partitioned array $\mathscr{V}$ is a field quantity comprised of the plastic strain, internal variable vector, stress, and plastic multiplier response

† Henceforth, vector notation[61] is used to represent the stress and strain tensor fields

fields at each Gauss point, i.e.

$$ {}^{n}\mathbf{v} = \begin{bmatrix} {}^{n}\boldsymbol{\varepsilon}_{\mathrm{p}} \\ {}^{n}\mathbf{p} \\ {}^{n}\boldsymbol{\tau} \\ {}^{n}\lambda \end{bmatrix} \tag{26} $$

By denoting ${}^{n}\mathbf{U}$ as the N-degree-of-freedom element nodal displacement vector, the N-dimensional array ${}^{n}\mathbf{R}$ is computed at each Gauss point from

$$ {}^{n}\mathbf{R}({}^{n}\mathbf{U}, {}^{n-1}\mathbf{U}, {}^{n}\mathbf{V}, {}^{n-1}\mathbf{v}, {}^{n}T, {}^{n-1}T) = \mathbf{B}^{\mathrm{T}}\,{}^{n}\boldsymbol{\tau}\, wJ - \mathbf{N}^{\mathrm{T}}\,{}^{n}\mathbf{b}\, wJ - \mathbf{N}^{\mathrm{T}n}\mathbf{t}\, wj \tag{27} $$

The matrices* $\mathbf{N}$ and $\mathbf{B}$ combine with ${}^{n}\mathbf{U}$ to interpolate the element displacement and strain fields, respectively.

If elastic behaviour or unloading occurs, then ${}^{n}\mathbf{v}$ reduces to ${}^{n}\mathbf{v} = [{}^{n}\boldsymbol{\tau}]$ and equation (17) is enforced pointwise by satisfying the residual

$$ {}^{n}\mathbf{H} = {}^{n-1}\boldsymbol{\tau} + \mathbf{C}[\mathbf{B}\,{}^{n}\mathbf{U} - \mathbf{B}^{n-1}\mathbf{U} - \alpha({}^{n}T)({}^{n}T - {}^{n-1}T)\mathbf{I}_{\tau}] - {}^{n}\boldsymbol{\tau} = \mathbf{0} \tag{28} $$

The above linear equation is trivially solved for ${}^{n}\boldsymbol{\tau}$. However, if neutral loading or plastic loading occurs, equations (15)–(17) and (20) are enforced pointwise at each Gauss point by satisfying the residual equation

$$ {}^{n}\mathbf{H}({}^{n}\mathbf{U}, {}^{n-1}\mathbf{U}, {}^{n}\mathbf{v}, {}^{n-1}\mathbf{v}, {}^{n}T, {}^{n-1}T) \equiv \begin{bmatrix} {}^{n}\mathbf{H}_{\varepsilon_{\mathrm{p}}} \\ {}^{n}\mathbf{H}_{\mathbf{p}} \\ {}^{n}\mathbf{H}_{\tau} \\ {}^{n}H_{\lambda} \end{bmatrix} = \mathbf{0} \tag{29} $$

where

$$ {}^{n}\mathbf{H}_{\varepsilon_{\mathrm{p}}} = {}^{n-1}\boldsymbol{\varepsilon}_{\mathrm{p}} + ({}^{n}\lambda - {}^{n-1}\lambda)\mathbf{f}({}^{n}\boldsymbol{\tau}, {}^{n}\mathbf{p}, {}^{n}T) - {}^{n}\boldsymbol{\varepsilon}_{\mathrm{p}} \tag{30} $$

$$ {}^{n}\mathbf{H}_{\mathbf{p}} = {}^{n-1}\mathbf{p} + ({}^{n}\lambda - {}^{n-1}\lambda)\mathbf{h}({}^{n}\boldsymbol{\tau}, {}^{n}\mathbf{p}, {}^{n}T) - {}^{n}\mathbf{p} \tag{31} $$

$$ {}^{n}\mathbf{H}_{\tau} = {}^{n-1}\boldsymbol{\tau} - {}^{n}\boldsymbol{\tau} + \mathbf{C}({}^{n}T)[\mathbf{B}\,{}^{n}\mathbf{U} - \mathbf{B}^{n-1}\mathbf{U} - {}^{n}\boldsymbol{\varepsilon}_{\mathrm{p}} + {}^{n-1}\boldsymbol{\varepsilon}_{\mathrm{p}} - \alpha({}^{n}T)({}^{n}T - {}^{n-1}T)\mathbf{I}_{\tau}] \tag{32} $$

$$ {}^{n}H_{\lambda} = Y({}^{n}\boldsymbol{\tau}, {}^{n}\mathbf{p}, {}^{n}T) \tag{33} $$

Equations (25) and (29) represent a non-linear transient coupled system which can be solved by implementing the coupled system Newton–Raphson procedure presented in References 16 and 65. In this procedure, equations (27) and (29) are uncoupled at each Gauss point by treating the response vector ${}^{n}\mathbf{v}$ as a function of the element nodal displacement vector ${}^{n}\mathbf{U}$. Two nested iterative loops are performed. The outer loop updates the Ith displacement vector estimate ${}^{n}\mathbf{U}^{I}$. In the inner loop, the current iterate ${}^{n}\mathbf{U}^{I}$ is fixed and ${}^{n}\mathbf{v}|_{{}^{n}\mathbf{U}^{I}}$ is evaluated via the Newton–Raphson process to satisfy equation (29).

For the Jth iterate of the inner loop ${}^{n}\mathbf{v}^{J}|_{{}^{n}\mathbf{U}^{I}}$, the incremental response $\delta\mathbf{v}$ is computed from

$$ \left.\frac{\partial {}^{n}\mathbf{H}}{\partial {}^{n}\mathbf{v}}\right|_{({}^{n}\mathbf{U}^{I}, {}^{n}\mathbf{v}^{J})} \delta\mathbf{v} = -{}^{n}\mathbf{H}|_{({}^{n}\mathbf{U}^{I}, {}^{n}\mathbf{v}^{J})} \tag{34} $$

* The matrices $\mathbf{N}$ and $\mathbf{B}$ are different from those appearing in the thermal analysis. Indeed, here they interpolate a vector field. However, the same notation is used to be consistent with the literature

where $\partial^n\mathbf{H}/\partial^n\mathbf{v}$ is deemed the dependent tangent operator. Upon evaluating the incremental response $\delta\mathbf{v}$, ${}^n\mathbf{v}|_{{}^n\mathbf{U}^I}$ is updated from the sum

$$ {}^n\mathbf{v}^{J+1}|_{{}^n\mathbf{U}^I} = {}^n\mathbf{v}^J|_{{}^n\mathbf{U}^I} + \delta\mathbf{v} \tag{35} $$

The inner loop Newton–Raphson subiterations are repeated until the solution ${}^n\mathbf{v}|_{{}^n\mathbf{U}^I}$ has conveged.

Once ${}^n\mathbf{v}|_{{}^n\mathbf{U}^I}$ is evaluated, the outer loop computations commence. The incremental response $\delta\mathscr{U}$ is computed by linearizing equation (25), i.e.

$$ \sum_{\text{elements}} \left\{ \sum_{\text{Gauss points}} \left[\frac{\partial^n\mathbf{R}}{\partial^n\mathbf{U}} \frac{\partial^n\mathbf{R}}{\partial^n\mathbf{v}} \overbrace{\left(\frac{\partial^n\mathbf{H}}{\partial^n\mathbf{v}}\right)^{-1}}^{-\frac{\partial^n\mathbf{v}}{\partial^n\mathbf{U}}} \frac{\partial^n\mathbf{H}}{\partial^n\mathbf{U}} \right] \Bigg|_{{}^n\mathbf{U}^I} \right\} \delta\mathscr{U} = - \sum_{\text{elements}} \left\{ \sum_{\text{Gauss points}} {}^n\mathbf{R}|_{{}^n\mathbf{U}^I} \right\} \tag{36} $$

where $\partial^n\mathbf{v}/\partial^n\mathbf{U} = -(\partial^n\mathbf{H}/\partial^n\mathbf{v})^{-1}\,\partial^n\mathbf{H}/\partial^n\mathbf{U}$ is derived by differentiating equation (29). The left-hand-side term in the above is deemed the independent tangent operator. Equation (36) is solved for $\delta\mathscr{U}$, and then the displacement vector ${}^n\mathscr{U}$ is updated from the sum

$$ {}^n\mathscr{U}^{I+1} = {}^n\mathscr{U}^I + \delta\mathscr{U} \tag{37} $$

The iteration–subiteration process is repeated for each iterate $\mathscr{U}^I$, until the solution ${}^n\mathscr{U}$ satisfies equation (25). At this point, the time is incremented and the process is repeated.

The operators $\partial^n\mathbf{R}/\partial^n\mathbf{U}$, $\partial^n\mathbf{R}/\partial^n\mathbf{v}$, $\partial^n\mathbf{H}/\partial^n\mathbf{U}$ and $\partial^n\mathbf{H}/\partial^n\mathbf{v}$ are computed at the Gauss points from

$$ \frac{\partial^n\mathbf{R}}{\partial^n\mathbf{U}} = \mathbf{0}_{N\times N} \tag{38} $$

$$ \frac{\partial^n\mathbf{R}}{\partial^n\mathbf{v}} = [\mathbf{0}_{N\times 6}\,\mathbf{0}_{N\times m}\,\mathbf{B}^{\mathrm{T}}\,wJ\,\mathbf{0}_{N\times 1}] \tag{39} $$

$$ \frac{\partial^n\mathbf{H}}{\partial^n\mathbf{U}} = \begin{bmatrix} \mathbf{0}_{6\times N} \\ \mathbf{0}_{m\times N} \\ \mathbf{CB} \\ \mathbf{0}_{1\times N} \end{bmatrix} \tag{40} $$

and

$$ \frac{\partial^n\mathbf{H}}{\partial^n\mathbf{v}} = \begin{bmatrix} \dfrac{\partial^n\mathbf{H}_{\varepsilon_p}}{\partial^n\boldsymbol{\varepsilon}_p} & \dfrac{\partial^n\mathbf{H}_{\varepsilon_p}}{\partial^n\mathbf{p}} & \dfrac{\partial^n\mathbf{H}_{\varepsilon_p}}{\partial^n\boldsymbol{\tau}} & \dfrac{\partial^n\mathbf{H}_{\varepsilon_p}}{\partial^n\lambda} \\ \dfrac{\partial^n\mathbf{H}_{\mathrm{p}}}{\partial^n\boldsymbol{\varepsilon}_p} & \dfrac{\partial^n\mathbf{H}_{\mathrm{p}}}{\partial^n\mathbf{p}} & \dfrac{\partial^n\mathbf{H}_{\mathrm{p}}}{\partial^n\boldsymbol{\tau}} & \dfrac{\partial^n\mathbf{H}_{\mathrm{p}}}{\partial^n\lambda} \\ \dfrac{\partial^n\mathbf{H}_{\tau}}{\partial^n\boldsymbol{\varepsilon}_p} & \dfrac{\partial^n\mathbf{H}_{\tau}}{\partial^n\mathbf{p}} & \dfrac{\partial^n\mathbf{H}_{\tau}}{\partial^n\boldsymbol{\tau}} & \dfrac{\partial^n\mathbf{H}_{\tau}}{\partial^n\lambda} \\ \dfrac{\partial^n H_{\lambda}}{\partial^n\boldsymbol{\varepsilon}_p} & \dfrac{\partial^n H_{\lambda}}{\partial^n\mathbf{p}} & \dfrac{\partial^n H_{\lambda}}{\partial^n\boldsymbol{\tau}} & \dfrac{\partial^n H_{\lambda}}{\partial^n\lambda} \end{bmatrix} $$

$$= \begin{bmatrix} -\mathbf{I}_{6\times 6} & ({}^{n}\lambda - {}^{n-1}\lambda)\dfrac{\partial \mathbf{f}}{\partial {}^{n}\mathbf{p}} & ({}^{n}\lambda - {}^{n-1}\lambda)\dfrac{\partial \mathbf{f}}{\partial {}^{n}\boldsymbol{\tau}} & \mathbf{f} \\ \mathbf{0}_{m\times 6} & ({}^{n}\lambda - {}^{n-1}\lambda)\dfrac{\partial \mathbf{h}}{\partial {}^{n}\mathbf{p}} - \mathbf{I}_{m\times m} & ({}^{n}\lambda - {}^{n-1}\lambda)\dfrac{\partial \mathbf{h}}{\partial {}^{n}\boldsymbol{\tau}} & \mathbf{h} \\ -\mathbf{C} & \mathbf{0}_{6\times m} & -\mathbf{I}_{6\times 6} & \mathbf{0}_{6\times 1} \\ \mathbf{0}_{1\times 6} & \dfrac{\partial Y}{\partial {}^{n}\mathbf{p}} & \dfrac{\partial Y}{\partial {}^{n}\boldsymbol{\tau}} & 0 \end{bmatrix} \tag{41}$$

2.2. Sensitivity analysis

In the sensitivity analysis, the residuals ${}^{n}\mathbf{W}$, ${}^{n}\mathbf{H}$ and ${}^{n}\mathbf{R}$, and the response fields ${}^{n}T$, ${}^{n}\mathbf{U}$ and ${}^{n}\mathbf{v}$ are expressed as functions of the design parameter vector ϕ. Consequently, equations (8), (25) and (29) are rewritten as

$$\sum_{\text{elements}} \left\{ \sum_{\text{Gauss points}} {}^{n}\mathbf{W}({}^{n}T(\phi), {}^{n-1}T(\phi), \phi \right\} = \mathbf{0} \tag{42}$$

$$\sum_{\text{elements}} \left\{ \sum_{\text{Gauss points}} {}^{n}\mathbf{R}({}^{n}\mathbf{U}(\phi), {}^{n-1}\mathbf{U}(\phi), {}^{n}\mathbf{v}(\phi), {}^{n-1}\mathbf{v}(\phi), {}^{n}T(\phi), {}^{n-1}T(\phi), \phi) \right\} = \mathbf{0} \tag{43}$$

$${}^{n}\mathbf{H}({}^{n}\mathbf{U}(\phi), {}^{n-1}\mathbf{U}(\phi), {}^{n}\mathbf{v}(\phi), {}^{n-1}\mathbf{v}(\phi), {}^{n}T(\phi), {}^{n-1}T(\phi), \phi) = \mathbf{0} \tag{44}$$

A general response functional F is defined at the final time* ${}^{M}t$ as

$$F(\phi) = G({}^{M}\mathcal{U}(\phi), {}^{M}\mathbf{v}(\phi), {}^{M}\mathcal{T}(\phi), \phi) \tag{45}$$

The response functional F may be used to quantify functionals which are defined as integral quantities over the domain V or at localized points of the domain, e.g. stress at a point or average stress. Differentiation of equation (45) with respect to each design parameter ϕ_i yields the following sensitivity expression:

$$\frac{DF}{D\phi_i} = \frac{\partial G}{\partial {}^{M}\mathcal{U}} \cdot \frac{D{}^{M}\mathcal{U}}{D\phi_i} + \frac{\partial G}{\partial {}^{M}\mathbf{v}} \cdot \frac{D{}^{M}\mathbf{v}}{D\phi_i} + \frac{\partial G}{\partial {}^{M}\mathcal{T}} \cdot \frac{D{}^{M}\mathcal{T}}{D\phi_i} + \frac{DG}{\partial \phi_i} \tag{46}$$

The derivatives $\partial G/\partial {}^{M}\mathcal{U}$, $\partial G/\partial {}^{M}\mathbf{v}$, $\partial G/\partial {}^{M}\mathcal{T}$ and $\partial G/\partial \phi_i$ are explicit quantities, whereas the derivatives $D{}^{M}\mathcal{T}/D\phi_i$, $D{}^{M}\mathcal{U}/D\phi_i$ and $D{}^{M}\mathbf{v}/D\phi_i$ are implicit quantities because ${}^{M}\mathcal{T}$ is determined through equation (42) and ${}^{M}\mathcal{U}$ and ${}^{M}\mathbf{v}$ are determined through equations (43) and (44).

The finite difference, direct differentiation or adjoint methods may be used for the resolution of the unknown implicit derivatives $D{}^{M}\mathcal{T}/D\phi_i$, $D{}^{M}\mathcal{U}/D\phi_i$ and $D{}^{M}\mathbf{v}/D\phi_i$. The direct differentiation method is incorporated in this study due to its efficiency over the finite difference method and due to algorithmic complications which arise in the transient adjoint method (cf. Reference 16).

The objective of the direct differentiation sensitivity is to evaluate the implicit derivatives $D{}^{M}\mathcal{T}/D\phi_i$, $D{}^{M}\mathcal{U}/D\phi_i$ and $D{}^{M}\mathbf{v}/D\phi_i$. Since equation (42) is independent of equations (43) and (44), a thermal sensitivity analysis is performed first to evaluate $D{}^{M}\mathcal{T}/D\phi_i$, and then the

* F may be defined on all time, but a terminal expression is assumed here for conciseness

mechanical sensitivities $D^M\mathscr{U}/D\phi_i$ and $D^M\mathbf{v}/D\phi_i$ are evaluated. Once $D^M\mathscr{T}/D\phi_i$, $D^M\mathscr{U}/D\phi_i$ and $D^M\mathbf{v}/D\phi_i$ are computed, the sensitivity of F is determined from equation (46).

2.2.1. Thermal sensitivity analysis. The thermal sensitivity analysis follows the procedure presented in References 32 and 33. At each time step n, the implicit response derivative $D^n\mathscr{T}/D\phi_i$ is evaluated by differentiating the global residual ${}^n\mathscr{W}$ (equation (43)), which after some manipulation becomes

$$\sum_{\text{elements}}\left\{\sum_{\text{Gauss points}}\frac{\partial {}^n\mathbf{W}}{\partial {}^n T}\right\}\frac{D^n\mathscr{T}}{D\phi_i} = -\sum_{\text{elements}}\left\{\sum_{\text{Gauss points}}\left(\frac{\partial {}^n\mathbf{W}}{\partial^{n-1}T}\frac{D^{n-1}T}{D\phi_i}+\frac{\partial^n W}{\partial\phi_i}\right)\right\} \tag{47}$$

In the above, the right-hand-side term forms the pseudo load and the left-hand-side operator is the tangent operator used for the Newton–Raphson iteration process (cf. equation (10)). This reappearance allows for the efficient computation of the response sensitivity $D^n\mathscr{T}/D\phi_i$. Indeed, the pseudo load vector is merely assembled followed by a back substitution into the previously decomposed tangent matrix. The formation of the pseudo load requires the derivative $D^{n-1}\mathscr{T}/D\phi_i$ which is computed at the previous time step. Note, however, that at the first time step $n = 1$, the design derivative of the initial condition $D^0\mathscr{T}/D\phi_i$ is known. Consequently, the derivatives $D^n\mathscr{T}/D\phi_i$ are merely evaluated in time with the primal solution so that all of the derivatives $D^{n-1}\mathscr{T}/D\phi_i$ are known.

2.2.2. Mechanical sensitivity analysis. The mechanical sensitivity analysis follows the methodology presented in Reference 16, where elastoplasticity is treated as a transient non-linear coupled problem. For the evaluation of the implicit derivatives $D^n\mathbf{U}/D\phi_i$ and $D^n\mathbf{v}/D\phi_i$, the derivative $D^n\mathbf{v}/D\phi_i$ is expressed as a function of the derivative $D^n\mathbf{U}/D\phi_i$. (Recall that ${}^n\mathbf{v}$ is expressed as a function of ${}^n\mathbf{U}$ in the solution process). Differentiation of equation (44) then yields

$$\begin{aligned}\frac{\partial {}^n\mathbf{H}}{\partial {}^n\mathbf{v}}\frac{D^n\mathbf{v}}{D\phi_i} = -\Bigg[&\frac{\partial {}^n\mathbf{H}}{\partial {}^n\mathbf{U}}\frac{D^n\mathbf{U}}{D\phi_i}+\frac{\partial {}^n\mathbf{H}}{\partial^{n-1}\mathbf{U}}\frac{D^{n-1}\mathbf{U}}{D\phi_i}\\&+\frac{\partial {}^n\mathbf{H}}{\partial^{n-1}\mathbf{v}}\frac{D^{n-1}\mathbf{v}}{D\phi_i}+\frac{\partial {}^n\mathbf{H}}{\partial {}^n T}\frac{D^n T}{D\phi_i}+\frac{\partial {}^n\mathbf{H}}{\partial^{n-1}T}\frac{D^{n-1}T}{D\phi_i}+\frac{\partial {}^n\mathbf{H}}{\partial\phi_i}\Bigg]\end{aligned} \tag{48}$$

Recall that the dependent tangent operator $\partial {}^n\mathbf{H}/\partial {}^n\mathbf{v}$ has been previously decomposed. The right-hand-side bracketed term forms the dependent pseudo load.

Differentiation of equation (43) and use of equation (48) yields

$$\begin{aligned}&\sum_{\text{elements}}\left\{\sum_{\text{Gauss points}}\left[\frac{\partial {}^n\mathbf{R}}{\partial {}^n\mathbf{U}}-\frac{\partial {}^n\mathbf{R}}{\partial {}^n\mathbf{v}}\left(\frac{\partial {}^n\mathbf{H}}{\partial {}^n\mathbf{v}}\right)^{-1}\frac{\partial {}^n\mathbf{H}}{\partial {}^n\mathbf{U}}\right]\right\}\frac{D^n\mathscr{U}}{D\phi_i}\\&\quad=-\sum_{\text{elements}}\left\{\sum_{\text{Gauss points}}\left[\frac{\partial {}^n\mathbf{R}}{\partial^{n-1}\mathbf{U}}\frac{D^{n-1}\mathbf{U}}{D\phi_i}+\frac{\partial {}^n\mathbf{R}}{\partial^{n-1}\mathbf{v}}\frac{D^{n-1}\mathbf{v}}{D\phi_i}\right.\right.\\&\qquad-\frac{\partial {}^n\mathbf{R}}{\partial {}^n\mathbf{v}}\left(\frac{\partial {}^n\mathbf{H}}{\partial {}^n\mathbf{v}}\right)^{-1}\left(\frac{\partial {}^n\mathbf{H}}{\partial\phi_i}+\frac{\partial {}^n\mathbf{H}}{\partial^{n-1}\mathbf{U}}\frac{D^{n-1}\mathbf{U}}{D\phi_i}\right.\\&\qquad+\frac{\partial {}^n\mathbf{H}}{\partial^{n-1}\mathbf{v}}\frac{D^{n-1}\mathbf{v}}{D\phi_i}+\frac{\partial {}^n\mathbf{H}}{\partial {}^n T}\frac{D^n T}{D\phi_i}+\frac{\partial {}^n\mathbf{H}}{\partial^{n-1}T}\frac{D^{n-1}T}{D\phi_i}\Bigg)\\&\qquad\left.\left.+\frac{\partial {}^n\mathbf{R}}{\partial {}^n T}\frac{D^n T}{D\phi_i}+\frac{\partial {}^n\mathbf{R}}{\partial^{n-1}T}\frac{D^{n-1}T}{D\phi_i}+\frac{\partial {}^n\mathbf{R}}{\partial\phi_i}\right]\right\}\end{aligned} \tag{49}$$

Here, recall that the operator on the left-hand side of the above equation is the independent tangent operator. The right-hand-side term forms the independent pseudo load.

The mechanical sensitivity analysis is analogous to the thermal sensitivity analysis. For each time step n, the primal analysis is performed to evaluate the global nodal displacement vector ${}^n\mathcal{U}$, and the field quantity ${}^n\mathbf{v}$ at each Gauss point. Next, the derivative $\partial {}^n\mathcal{U}/\partial\phi_i$ is computed from equation (49) by forming the independent pseudo load and back substituting using the previously decomposed independent stiffness matrix from equation (36). Then, the derivative $\partial {}^n\mathbf{v}/\partial\phi_i$ at each Gauss point is computed from equation (48) by forming the dependent pseudo load and back substituting using the previously decomposed dependent matrix (cf. equation (34)). The process is repeated for each design parameter ϕ_i.

The operators $\partial {}^n\mathbf{R}/\partial {}^nT$ and $\partial {}^n\mathbf{H}/\partial {}^nT$ for each Gauss point are computed as

$$\frac{\partial {}^n\mathbf{R}}{\partial {}^nT} = \mathbf{0}_{N\times 1} \tag{50}$$

and

$$\frac{\partial {}^n\mathbf{H}}{\partial {}^nT} = \begin{bmatrix} ({}^n\lambda - {}^{n-1}\lambda)\dfrac{\partial \mathbf{f}}{\partial {}^nT} \\ ({}^n\lambda - {}^{n-1}\lambda)\dfrac{\partial \mathbf{h}}{\partial {}^nT} \\ \dfrac{\partial \mathbf{C}}{\partial {}^nT}[\mathbf{B}{}^n\mathbf{U} - \mathbf{B}{}^{n-1}\mathbf{U} - {}^n\boldsymbol{\varepsilon}_p + {}^{n-1}\boldsymbol{\varepsilon}_p - \alpha({}^nT - {}^{n-1}T)\mathbf{I}_\tau] \\ \quad - \mathbf{C}\left[\dfrac{\partial \alpha}{\partial {}^nT}({}^nT - {}^{n-1}T) + \alpha\right]\mathbf{I}_\tau \\ \dfrac{\partial Y}{\partial {}^nT} \end{bmatrix} \tag{51}$$

and the operators

$$\frac{\partial {}^n\mathbf{R}}{\partial {}^{n-1}\mathbf{U}}, \frac{\partial {}^n\mathbf{R}}{\partial {}^{n-1}\mathbf{v}}, \frac{\partial {}^n\mathbf{R}}{\partial {}^{n-1}T}, \frac{\partial {}^n\mathbf{H}}{\partial {}^{n-1}\mathbf{U}}, \frac{\partial {}^n\mathbf{H}}{\partial {}^{n-1}\mathbf{v}}, \text{ and } \frac{\partial {}^n\mathbf{H}}{\partial {}^{n-1}T},$$

as

$$\frac{\partial {}^n\mathbf{R}}{\partial {}^{n-1}\mathbf{U}} = \mathbf{0}_{N\times N} \tag{52}$$

$$\frac{\partial {}^n\mathbf{R}}{\partial {}^{n-1}\mathbf{v}} = \mathbf{0}_{N\times(6+m+6+1)} \tag{53}$$

$$\frac{\partial {}^n\mathbf{R}}{\partial {}^{n-1}T} = \mathbf{0}_{N\times 1} \tag{54}$$

$$\frac{\partial {}^n\mathbf{H}}{\partial {}^{n-1}\mathbf{U}} = \begin{bmatrix} \mathbf{0}_{6\times N} \\ \mathbf{0}_{m\times N} \\ \mathbf{CB} \\ \mathbf{0}_{1\times N} \end{bmatrix} \tag{55}$$

$$\frac{\partial^n \mathbf{H}}{\partial^{n-1}\mathbf{v}} = \begin{bmatrix} \mathbf{I}_{6\times 6} & \mathbf{0}_{6\times m} & \mathbf{0}_{6\times 6} & -\mathbf{f} \\ \mathbf{0}_{m\times 6} & \mathbf{I}_{m\times m} & \mathbf{0}_{m\times 6} & -\mathbf{h} \\ \mathbf{C} & \mathbf{0}_{6\times m} & \mathbf{I}_{6\times 6} & \mathbf{0}_{6\times 1} \\ \mathbf{0}_{1\times 6} & \mathbf{0}_{1\times m} & \mathbf{0}_{1\times 6} & 0 \end{bmatrix} \tag{56}$$

$$\frac{\partial^n \mathbf{H}}{\partial^{n-1} T} = \begin{bmatrix} \mathbf{0}_{6\times 1} \\ \mathbf{0}_{m\times 1} \\ \mathbf{C}\alpha\mathbf{I}_\tau \\ 0 \end{bmatrix} \tag{57}$$

In equation (49), the derivative $\partial^n T/\partial\phi_i$ is computed in the thermal sensitivity analysis. The quantities $\partial^n \mathbf{H}/\partial\phi_i$ and $\partial^n \mathbf{R}/\partial\phi_i$ are explicit and depend on the parametrization of ϕ.

3. WELDMENT DESIGN OPTIMIZATION

The weakly coupled thermoelastoplastic analysis and sensitivity analysis are combined with numerical optimization to form an optimum design algorithm. A butt weldment is optimized to demonstrate the algorithm. For each optimization iteration, both manufacturing and service analyses are performed. In the manufacturing analysis, a thermal analysis and a thermal sensitivity analysis are initially performed to compute the thermal field and its sensitivity. Then, the mechanical analysis and mechanical sensitivity analysis commence, to determine the thermal-induced residual stress and its sensitivity. For the simulation of the product's service environment, the structure is subsequently loaded and sensitivites of the service stresses are computed. This information is used by the optimization algorithm to update the design. The optimization iterates until it converges to an optimum.

3.1. Problem statement

The analysis models both the manufacturing process and the product's service. In the manufacturing process, two beads are simultaneously deposited on a 0·23 per cent carbon mild steel rectangular plate—see Figure 1. The welding direction is perpendicular to the plane of the figure

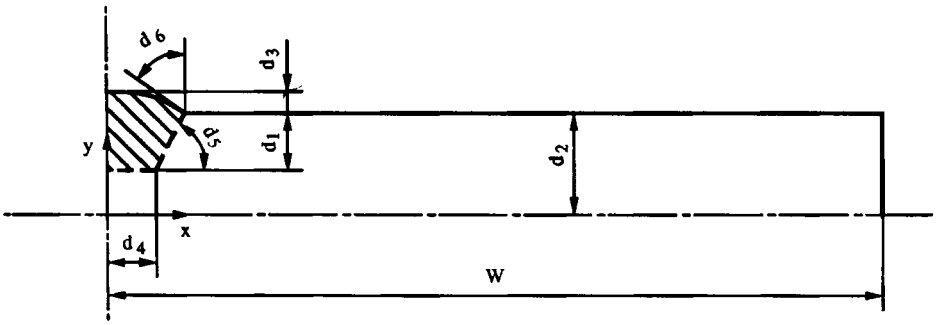

Figure 1. Butt weldment

and the shaded region represents the filler metal, also mild steel. After the plate has cooled, it is loaded with a tensile load $P = 7 \times 10^5$ N on the edges to simulate the product service load (cf. Figure 11).

Because of symmetry, only a quarter of the plate is modelled. The same finite element mesh is used for both thermal and mechanical analyses. It consists of 552 quadrilateral 8-noded elements—see Figure 2. The mesh is parametrized using PATRAN[66] and a command language program (PCL[67])—see Reference 33. The shape of the welded plate is described by six shape parameters (d_1–d_6)—see Figure 1. The plate half-width W and length L are fixed at 140 and 100 mm, respectively.

The optimization problem is to determine the plate half-thickness d_2, weldment shape and weldment parameters that minimize the weight of the welded loaded plate and simultaneously limit the von Mises stress level to 420 MPa. The cost functional is equal to the volume of the welded plate. The design parameter vector consists of the six shape parameters (see Figure 1), as well as the welding energy input rate Q, and the torch speed v (see equation (58)). The initial values of the design parameters, their upper and lower bounds, and their optimum values appear in Table I.

3.2. *Thermal analysis*

The thermal analysis is performed in the plane normal to the welding direction by assuming that the heat flow in the welding direction is negligible. This is a reasonable assumption for high welding speeds (cf. Reference 44). The internal heat generation r for the weldment is modelled by the double ellipsoid heat source model of Reference 49,

$$r = \frac{6\sqrt{3}Qf}{abc\pi\sqrt{\pi}} e^{-\left\{\frac{3x^2}{a^2}\frac{3(d_2-y)^2}{b^2}+\frac{3[z+v(\tau-t)]^2}{c^2}\right\}} \tag{58}$$

where a, b and c are the ellipsoid semiaxes, t is the time and τ is a lag factor defined by the position

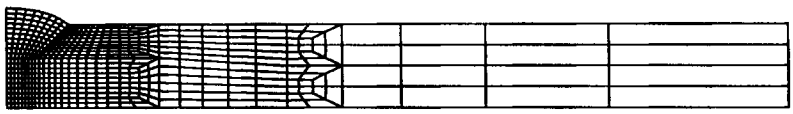

Figure 2. Finite element mesh

Table I. Design parameter values of the weldment design optimization problem

Design parameter	Initial value	Upper bound	Lower bound	Optimum value
d_1 (mm)	6·00	8·00	4·00	4·97
d_2 (mm)	15·00	20·00	10·00	10·00
d_3 (mm)	3·00	5·00	1·50	1·50
d_4 (mm)	5·00	8·00	3·00	3·29
d_5 (degrees)	45·00	30·00	60·00	30·00
d_6 (degrees)	50·00	70·00	0·00	69·64
Q (W)	32 000·00	100 000·00	1000·00	9531·73
v (mm/s)	6·00	10·00	2·00	4·96

of the torch at time $t = 0$; f is an empirical coefficient equated to 0·6 and 1·6 ahead of and behind the torch, respectively (cf. Reference 49). The energy input rate Q, is evaluated from

$$Q = \eta VI \tag{59}$$

where η, V and I are the heat source efficiency, voltage and current, respectively.

The ellipsoid semiaxes a, b and c are defined as (cf. Reference 49)

$$a = d_4 + d_2 \tan(d_5) \tag{60}$$

$$b = d_1 \tag{61}$$

$$c = \begin{cases} a & \text{ahead of the torch} \\ 4a & \text{behind the torch} \end{cases} \tag{62}$$

Zero power distribution is defined on the weldment reinforcement (i.e. $r = 0$ for $y > d_2$) to conserve the global energy*. Moreover, it is assumed that the filler metal is deposited on the plate ahead of the torch (i.e. both filler and base metal are heated simultaneously).

A uniform, initial temperature distribution of 20°C is assumed. Convective–radiative boundary conditions are assigned over the sides and edges of the plate (see Figure 3). The surface flux q^s for the convective–radiative boundary is given by

$$q^s = [\hbar + \sigma\varepsilon(T^2 + T_\infty)(T + T_\infty)](T - T_\infty) \tag{63}$$

where $\hbar$ is the convection coefficient, ε is the emissivity, σ is the Stefan–Boltzman constant and T_∞ is the ambient temperature.† For the present work, $\hbar = 150 \times \text{W/m}^2/°\text{C}$, $\varepsilon = 0{\cdot}8$ (cf. Reference 68) and $T_\infty = 293$ K.

The temperature-dependent thermal conductivity k and enthalpy h are plotted in Figures 4 and 5, respectively. Thermal conductivity data for mild steel are taken from BISRA. For temperatures above 1300°C, pure iron data from Wray[68] are used, noting that at elevated temperatures, the influence of alloying content on the thermal conductivity is insignificant (cf. Reference 68). For temperatures above melting (1482°C), the thermal conductivity is artificially raised to $k = 120\text{W/m/°C}$ to simulate the convective heat transfer of the molden pool (cf. Reference 49). Enthalpy data are taken from BISRA.[69] For temperatures above 1300°C, the temperature-dependent enthalpy function is constructed by integrating the pure iron specific heat data of Reference 70. The enthalpy curve exhibits a latent heat of fusion of 247×10^3 J/Kg/°C (cf.

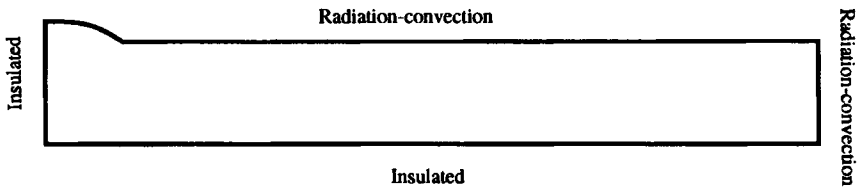

Figure 3. Thermal analysis boundary conditions

* The weldment reinforcement is ignored in the derivation of the exponential coefficients for the double ellipsoid model of equation (58) (cf. Reference 49). Non-zero internal heat generation on the reinforcement would violate the global energy conservation

† T and T_∞ in equation (63) are expressed in K

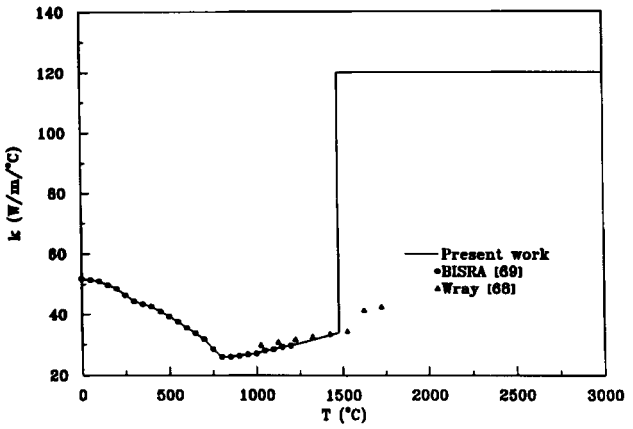

Figure 4. Thermal conductivity of mild steel

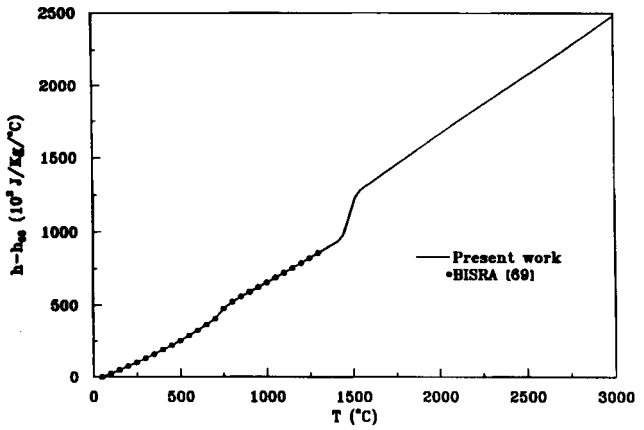

Figure 5. Enthalpy of mild steel

Reference 70). The mass density is taken at room temperature and is held constant at $\rho = 7{\cdot}86 \times 10^3$ kg/m^3 (BISRA[69]).

An enhanced version of the finite element package FIDAP[32,33,71] is used to compute the temperature field and its sensitivity. The time domain is discretized in 35 variable steps. The time step size is controlled by a local time truncation error algorithm (cf. Reference 71). The peak temperature contours obtained throughout the heat cycle of the initial design appear in Figure 6. Their sensitivities with respect to the plate half thickness d_2 and energy input rate Q are shown in Figures 7 and 8, respectively. As seen from these figures, the peak temperatures decrease by increasing the plate half-thickness d_2, and increase by increasing the energy input rate Q.

The analytically computed sensitivities are validated by also computing the sensitivities by the costly forward finite difference method.[72] It is well known that round-off and truncation errors affect the accuracy of the finite difference approximations, especially when the sensitivities are relatively small. For the correlation of the finite difference and analytic sensitivity computations,

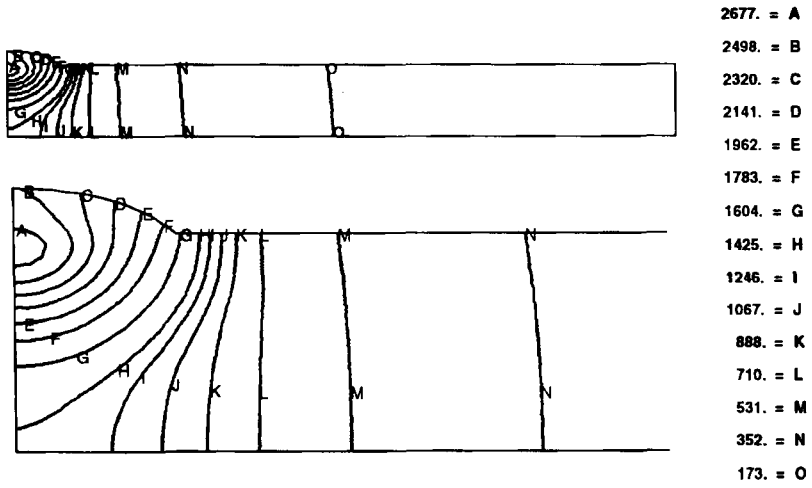

Figure 6. Peak temperatures of the initial design

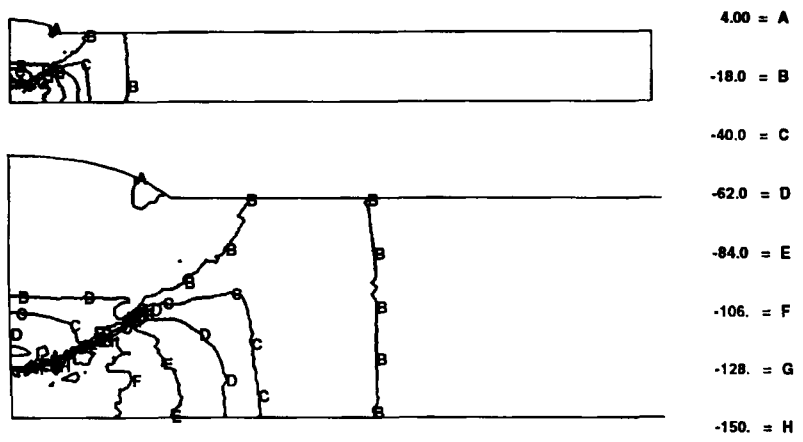

Figure 7. Peak temperature sensitivity of the initial design with respect to d_2

a percentage discrepancy is defined as

$$\text{Percentage discrepancy} = \text{absolute value}\left(\frac{\text{analytic sensitivity} - \text{finite difference sensitivity}}{\text{finite difference sensitivity}}\right) * 100$$

The correlation between the two methods is excellent as seen in the percentage discrepancy Figures 9 and 10. The discrepancy is localized to the regions where the sensitivities are relatively small. Over the majority of the domain, the percentage discrepancy is of the order 10^{-2}.

3.3. Mechanical analysis

The plane strain assumption is used to model the welding process and subsequent service loading. Rate-independent, elastoplastic material response with isotropic hardening is assumed. The present

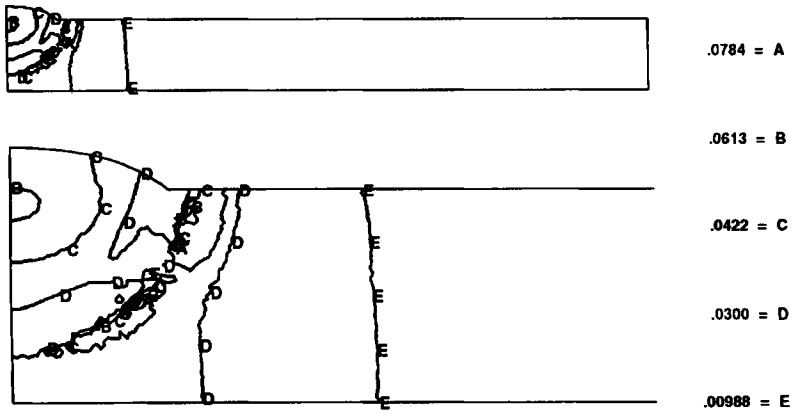

Figure 8. Peak temperature sensitivity of the initial design with respect to Q

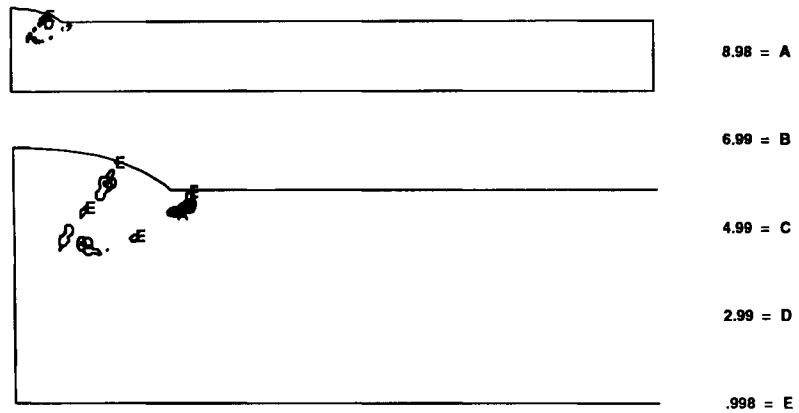

Figure 9. Percentage discrepancy between the finite difference and analytic peak temperature sensitivity with respect to d_2

model does not include solid state transformations (cf. References 44, 48, 55–57). The small deformation isotropic hardening model is inadequate to evaluate the plastic hardening at high temperatures; therefore, it is assumed that no further hardening occurs for temperatures exceeding 600°C. This assumption does not significantly affect the residual stress computations, since plastic strain energy is negligible at high temperatures.[53]

The yield function Y, is given by

$$Y = \tau_p - (\tau_y + E_p e_p) \tag{64}$$

where τ_y is the initial yield limit, E_p is the plastic modulus, and τ_p and $e_p = \int \dot{e}_p \, dt$ are the equivalent plastic stress and strain, respectively,*

$$\tau_p \equiv \sqrt{\tfrac{3}{2} s_i s_i} \tag{65}$$

*Summation convention is enforced on repeated indices

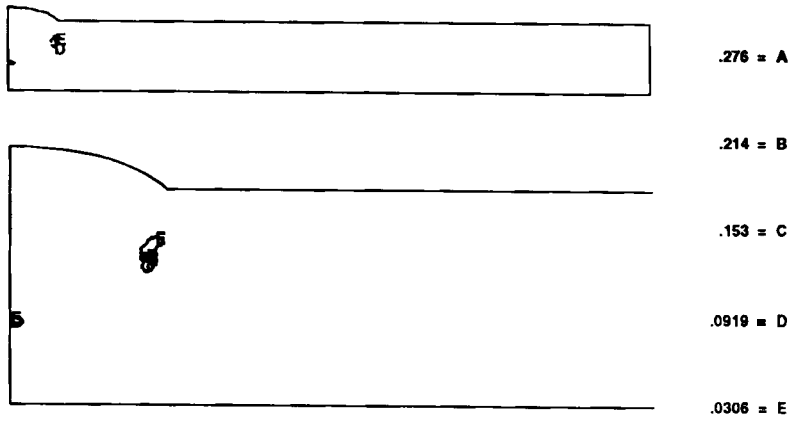

Figure 10. Percentage discrepancy between the finite difference and analytic peak temperature sensitivity with respect to Q

Figure 11. Mechanical analysis boundary conditions

and

$$\dot{e}_p \equiv \sqrt{\tfrac{2}{3}\dot{\varepsilon}_{p_i}\dot{\varepsilon}_{p_i}} \tag{66}$$

Here, s_i are the deviatoric stress components

$$s_i \equiv \begin{cases} \tau_i - \frac{1}{3}(\tau_1 + \tau_2 + \tau_3) & \text{for } i = 1,2,3 \\ \tau_i & \text{for } i = 4,5,6 \end{cases} \tag{67}$$

The boundary conditions and loading are illustrated in Figure 11.

The temperature-dependent mechanical material properties are plotted in Figures 12–16. The Young's modulus data are taken from Michel[73] (0·25 per cent carbon steel, below 600°C, dynamic loading) and from Mizukami[74] (above 600°C, $\dot{\varepsilon} = 3 \times 10^{-3}$ 1/s), see Figure 12. For comparison purposes, data from Hill[75] (SAE 1020) and Wray[68] (unrelaxed pure iron) are also plotted in Figure 12. The Young's modulus data are stress-rate dependent; however, the strain rates are typically in the range $\dot{\varepsilon} = 10^{-3}$–$10^{-2}$ 1/s for this example. Data for the initial yield limit τ_y are taken from Smithells[76] (0·25 per cent carbon steel, below 500°C), see Figure 13. The plastic modulus E_p data are taken from Mizukami,[74] see Figure 14. The temperature variation of differential thermal expansion coefficient α is constructed from the mean coefficient data of BISRA[69] (0·23 per cent carbon steel, below 1200°C). For temperatures above 1200°C, the differential thermal expansion coefficient given by Wray[68] for pure iron is used. The Poisson's ratio ν is taken from Michel[73] where extrapolation is used at temperatures exceeding 1100°C. The effect of Poisson's ratio on the residual stress field is negligible at the high temperatures of the extrapolated region (cf. Reference 54).

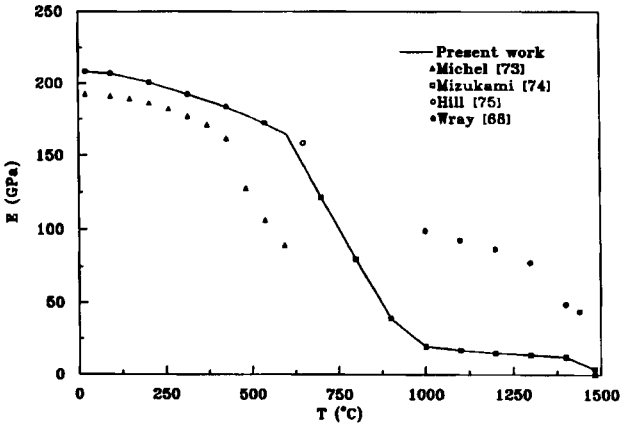

Figure 12. Variation of Young's modulus with temperature

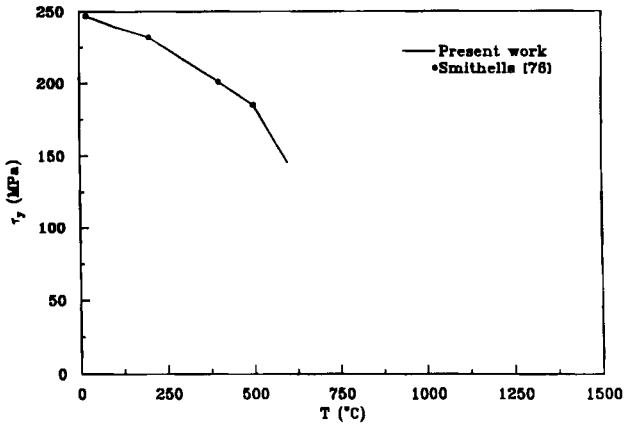

Figure 13. Variation of yield stress with temperature

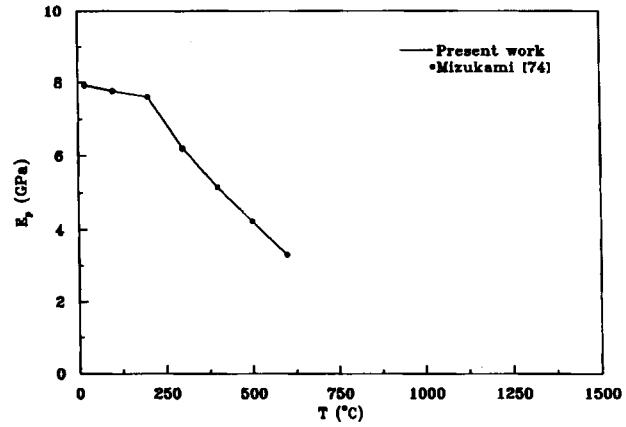

Figure 14. Variation of plastic modulus with temperature

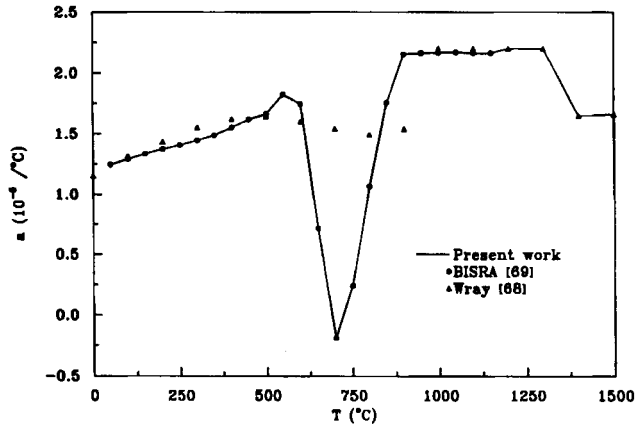

Figure 15. Variation of differential thermal expansion coefficient with temperature

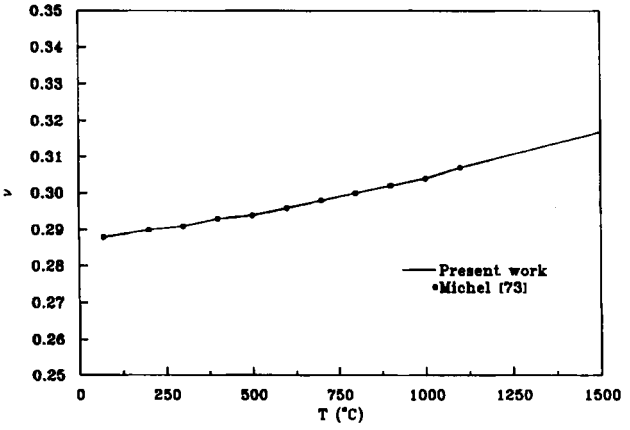

Figure 16. Variation of Poisson's ratio with temperature

The quasi-static residual stress analysis uses the same time discretization as the transient thermal analysis. Additional quasi-static steps are used to analyse the service load application.

The same finite element mesh is used throughout the analysis. For the simulation of the filler metal deposition, a small value for the Young's modulus and a large initial yield limit value are assigned to the filler metal before deposition. In this way, in the filler metal region the stress is essentially zero before deposition. Base metal properties are assigned to the filler metal elements as their temperatures drops below the solidification temperature.

The contour plots of Figures 17 and 18 illustrate the computed von Mises residual and service stress fields of the initial design, respectively. A peak residual stress of 443 MPa and service stress of 448 MPa are predicted. The sensitivities of the von Mises residual and service stress fields with respect to the plate half thickness d_2 and the energy input rate Q are shown in Figures 19–22. As seen in these figures, the von Mises residual and service stresses increase in the region of the peak von Mises stress, as the plate thickness increases. Elsewhere, in general, they decrease. The von Mises residual and service stresses will, in general, increase as the energy input rate Q increases.

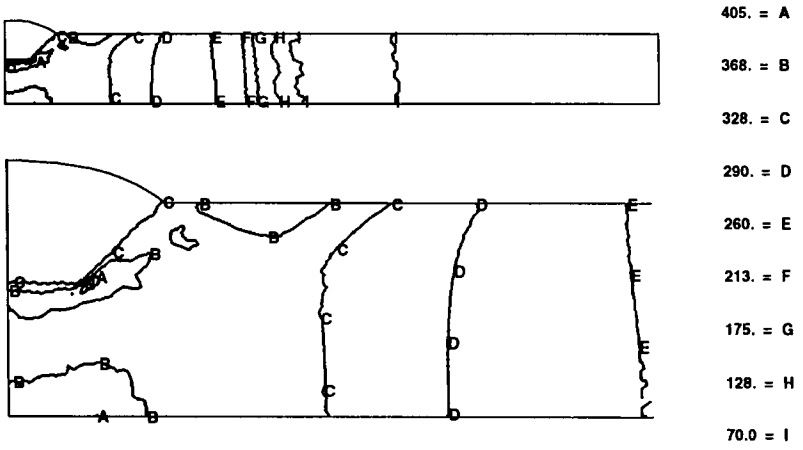

Figure 17. von Mises residual stress

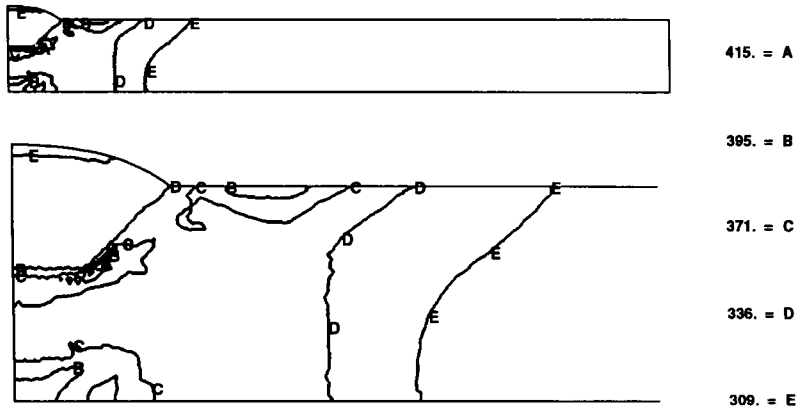

Figure 18. von Mises service stress

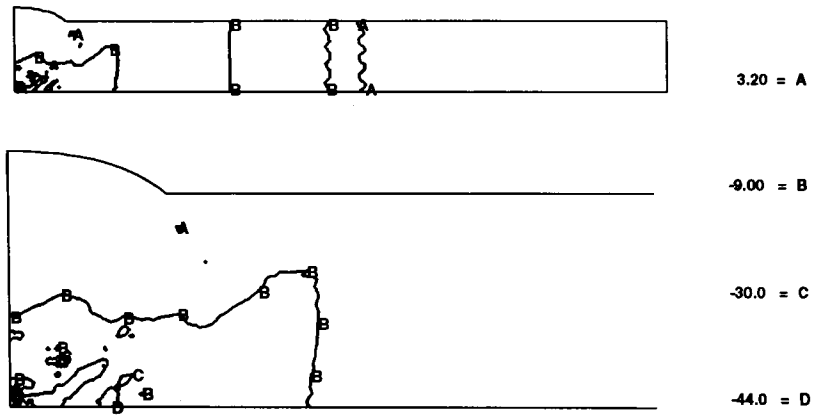

Figure 19. von Mises residual stress sensitivity with respect to d_2

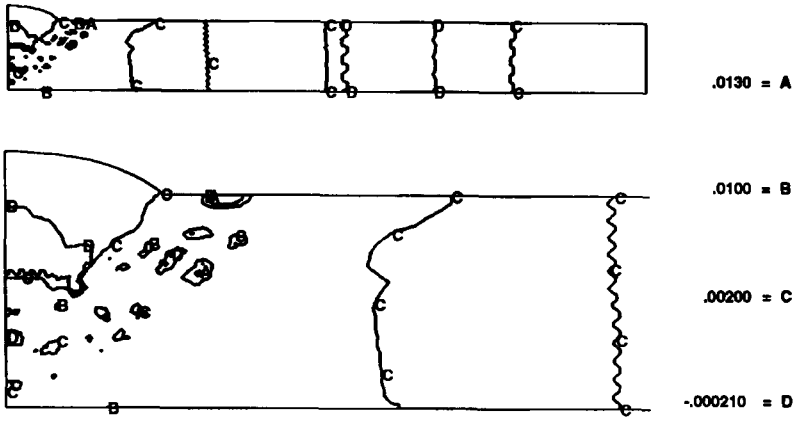

Figure 20. von Mises residual stress sensitivity with respect to Q

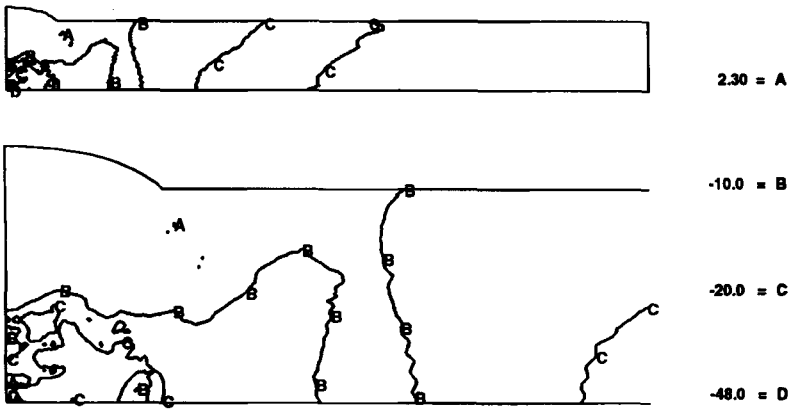

Figure 21. von Mises service stress sensitivity with respect to d_2

The analytically computed mechanical sensitivities are also validated with finite difference sensitivities in a manner analogous to the thermal sensitivity analysis. Again, with the exception of the regions with small sensitivities, the correlation between the two methods is excellent as seen in the present discrepancy Figures 23 and 24.

3.4. Design optimization

An optimization is performed to minimize the weld mass and constrain the peak temperature and von Mises stress levels which develop during the manufacturing process and product service loading.

Constraints are defined to ensure that the heat input is sufficient to perform the welding. These constraints require the peak nodal temperatures of the filler metal to exceed 1482°C. To limit filler metal evaporation during the welding, additional constraints restrict the peak nodal temperatures of the filler metal to be less than 3000°C.

The 420 MPa von Mises stress level limit, enforced over the entire structure, defines the remaining constraints for the optimization problem. The total number of stress constraints is reduced and the

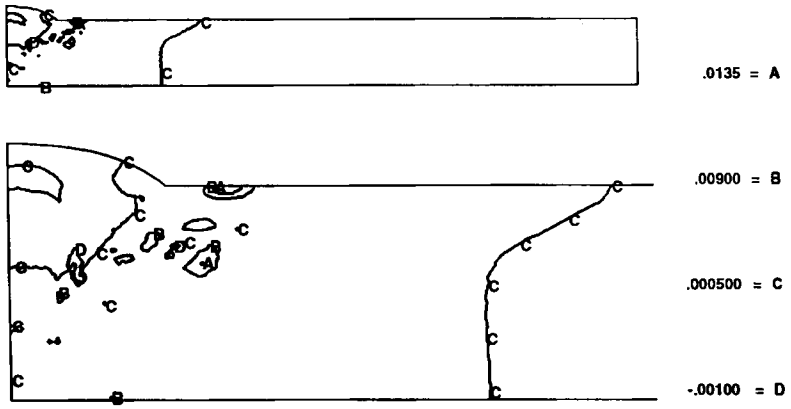

Figure 22. von Mises service stress sensitivity with respect to Q

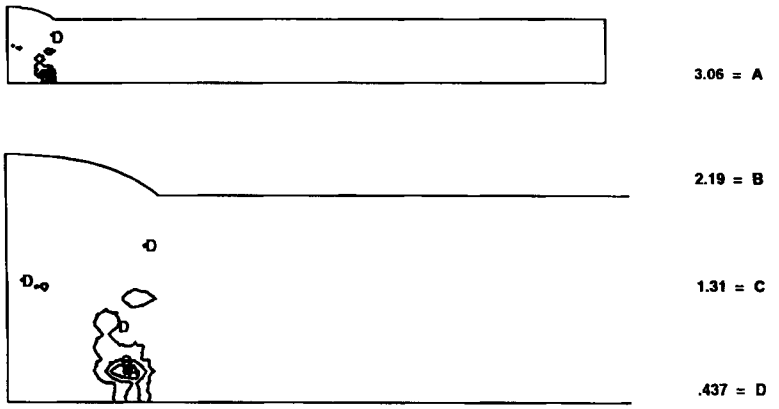

Figure 23. Percentage discrepancy between the finite difference and analytic von Mises residual stress sensitivity with respect to d_2

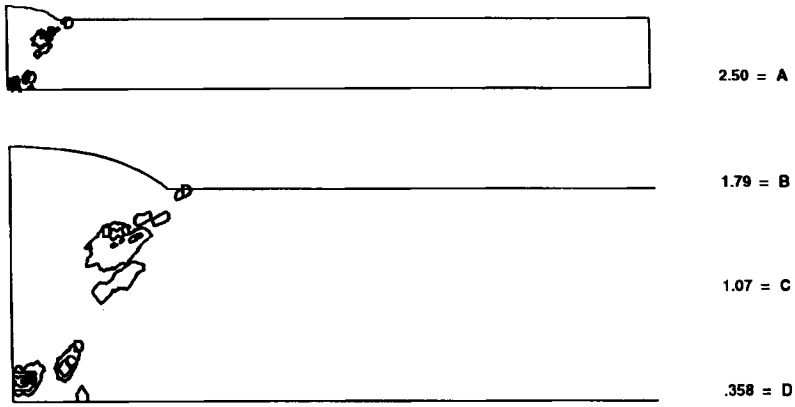

Figure 24. Percentage discrepancy between the finite difference and analytic von Mises service stress sensitivity with respect to Q

optimization efficiency is improved by using the mean von Mises stress of each element rather than the individual element Gauss point stress.

The numerical optimization is performed with the sequential linear programming algorithm of DOT.[77] Nine sensitivity analyses and fourteen analyses are required to obtain convergence. Each sensitivity analysis requires 10 per cent of the analysis CPU time. The optimum values of the design parameters are denoted in Table I. Most of the design parameters attain their minimum or maximum allowable values (see Table I). The objective function, i.e. the welded plate area, is reduced from 2124 to 1406 mm^2. The peak temperature contours throughout the heat cycle and the von Mises residual and service stress contour of the optimum design are illustrated in Figures 25–27, respectively. The peak von Mises residual stress in reduced to 411 MPa and the peak von Mises service stress is reduced to 413 MPa. Note that only those constraints related to the peak temperature field remain active at the optimum configuration.

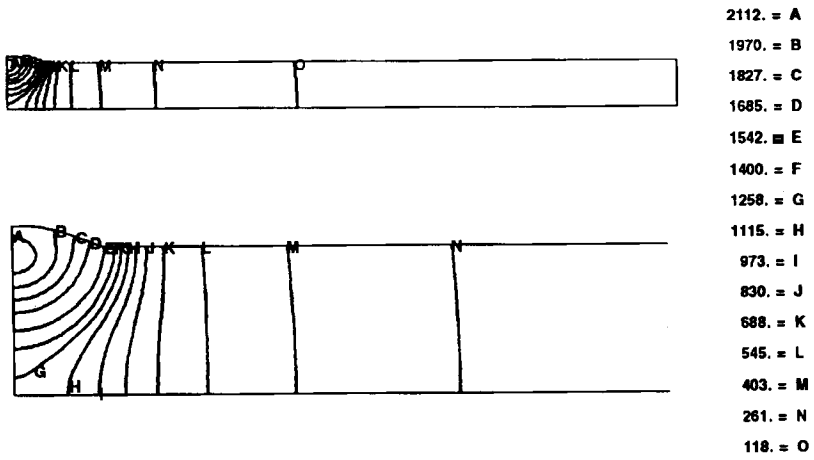

Figure 25. Peak temperatures of the final design

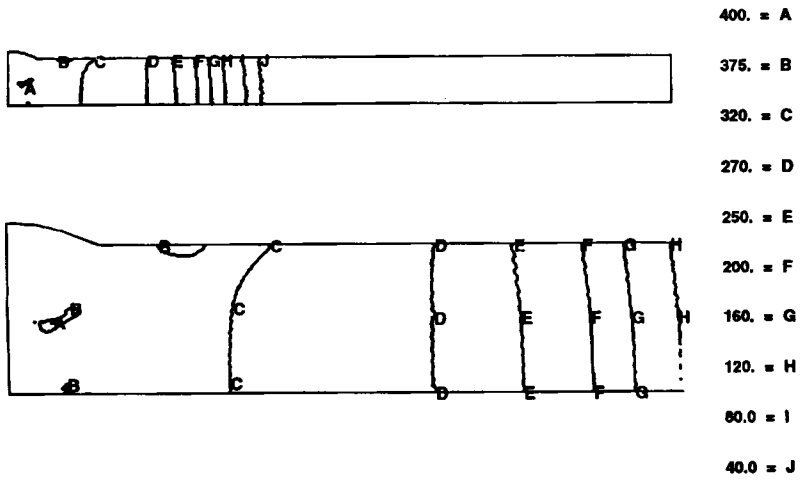

Figure 26. von Mises residual stress of the optimum design

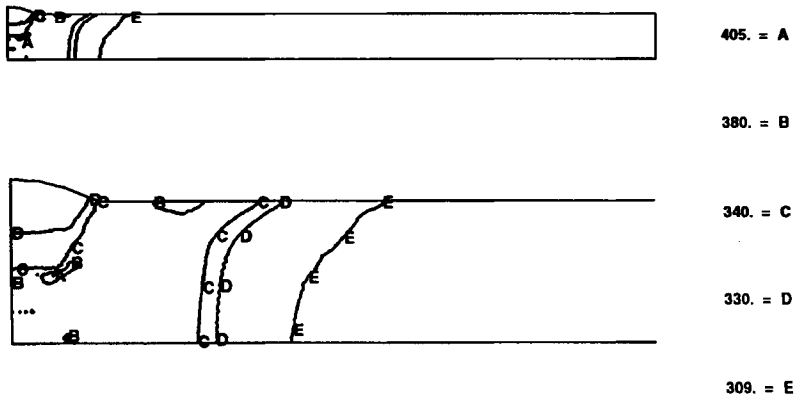

Figure 27. von Mises service stress of the optimum design

4. CONCLUSION

A systematic design approach for systems governed by transient thermo elastoplastic problems is presented. The approach utilizes numerical optimization, the finite element method, and analytic sensitivity analysis. The solution of weakly coupled thermoelastoplastic systems with the Newton–Raphson iteration method is also discussed. Analytic sensitivities are formulated with the direct differentiation method. The analysis and sensitivity analysis capabilities are finally combined with numerical optimization to form an optimum design algorithm.

The design of a weldment demonstrates the efficiency of the algorithm. The residual stresses which evolve during the heat cycle of the welding process are predicted by solving a nonlinear transient thermoelastoplastic problem. The product's service environment is simulated by subsequently loading and analysing the structure. The weldment shape, energy input rate, and the torch speed are optimized to minimize the structure's weight and simultaneously limit the von Mises stress level.

ACKNOWLEDGMENT

The studies presented here were conducted under the support of the Edison Welding Institute for the project 8.5.2/13UIE1198 and the National Science Foundation through contract NSF DDM93-58/32NYI.

REFERENCES

1. R. J. Yang, K. K. Choi and E. J. Haug, 'Numerical considerations in structural component shape optimization', *Trans. ASME*, **107**, 334–339 (1985).
2. A. D. Belegundu and S. D. Rajan, 'A shape optimization approach based on natural design variables and shape functions', *Comput. Methods Appl. Mech. Eng.*, **66**, 87–106 (1988).
3. S. D. Rajan and A. D. Belegundu, 'Shape optimal design using fictitious loads, *AIAA J.*, **27**, 102–107 (1988).
4. V. B. Venkayya, 'Structural optimization: a review and some recommendations', *Int. j. numer. methods eng.*, **13**, 203–228 (1978).
5. E. J. Haug, K. K. Choi and V. Komkov, *Design Sensitivity Analysis of Structural Sytems*, Academic Press, New York, 1986.
6. Z. Mroz, M. P. Kamat and R. H. Plaut, 'Sensitivity analysis and optimal design of nonlinear beams an plates', *J. Struct. Mech.*, **13**, 245–266 (1985).
7. R. T. Haftka and Z. Mroz, 'First- and second-order sensitivity analysis of linear and nonlinear structures', *AIAA J.* **24**, 1187–1192 (1986).

8. K. K. Choi and J. L. T. Santos, 'Design sensitivity analysis of nonlinear structural systems. Part I. 'Theory', *Int. j. numer. methods eng.*, **24**, 2039–2055 (1987).
9. C. C. Wu and J. S. Arora, 'Design sensititvity analysis and optimization of nonlinear structural response using incremental procedure', *AIAA J.*, **25**, 1118–1125 (1987).
10. J. L. T. Santos and K. K. Choi, 'Sizing design sensitivity analysis of nonlinear structural systems. Part-II. Numerical method', *Int. j. numer. methods eng.*, **26**, 2097–2114 (1988).
11. G. Szefer, Z. Mroz and L. Dembowicz, 'Variational approach to sensitivity analysis in nonlinear elasticity', *Arch. Mech.*, **39**, 247–259 (1987).
12. J. B. Cardoso and J. S. Arora, 'Variational method for design sensitivity analysis in nonlinear structural mechanics', *AIAA J.*, **26**, 595–603 (1988).
13. H. S. Gopalakrishna and L. F. Greimann, 'Newton–Raphson procedure for the sensitivity analysis of nonlinear structural behavior', *Comput. Struct.*, **30**, 1263–1273 (1988).
14. D. G. Phelan, C. Vidal and R. B. Haber, 'An adjoint variable method for sensitivity analysis of nonlinear elastic systems', *Int. j. numer. methods eng.*, **31**, 1649–1667 (1991).
15. D. A. Tortorelli, 'Sensitivity analysis for non-linear constrained elastostatic systems', *Int. j. numer. methods eng.*, **33**, 1643–1660 (1992).
16. P. Michaleris, D. A. Tortorelli and C. A. Vidal, 'Tangent operators and design sensitivity formulations for transient nonlinear coupled problems with applications to elasto-plasticity', *Int. j. numer. methods eng.*, **37**, 2471–2499 (1994).
17. M. P. Bendsoe and J. Sokolowski, 'Sensitivity analysis and optimization of elastic–plastic structures', *Eng. Optim.*, **11**, 31–38 (1987).
18. M. P. Bendsoe and J. Sokolowski, 'Design sensitivity analysis of elastic–plastic analysis problems', *Mech. Struct. Mach.*, **16**, 81–102 (1988).
19. J. J. Tsay and J. S. Arora, 'Nonlinear structural design sensitivity analysis for path dependent problems. Part 1. General theory', *Comput. Methods Appl. Mech. Eng.*, **81**, 183–208 (1990).
20. J. J. Tsay, J. E. B. Cardoso and J. S. Arora, 'Nonlinear structural design sensitivity analysis for path dependent problems. Part 2. Analytic examples', *Comput. Methods Appl. Mech. Eng.*, **81**, 209–228 (1990).
21. Q. Zhang and S. Mukherjee, 'Design sensitivity coefficients for elastic-viscoplastic problems by boundary element methods', *Int. j. numer. methods eng.*, **34**, 947–966 (1992).
22. M. Kleiber, T. D. Hien and E. Postek, 'Incremental finite element analysis of nonlinear structural design sensitivity problems', in E. Onate, J. Periaux and A. Samuelsson, (eds.), *Finite Elements in the 90's*, Barcelona, Springer-Verlag/CIMNE, 1991, pp. 241–247.
23. C. A. Vidal and R. B. Haber, 'Design sensitivity analysis for rate-independent elastoplasticity', *Comput. Methods Appl. Mech. Eng.*, **107**, 393–431 (1993).
24. R. B. Haber, D. A. Tortorelli, C. A. Vidal, and D. G. Phelan, 'Design sensitivity analysis of nonlinear structures—I: Large-deformation hyperelasticity and history-dependent material response', In M. P. Kamat, (ed.), *Structural Optimization: State and Promise*, AIAA Progress in Astronautics and Aeronautics series, 1993, pp. 369–406.
25. R. A. Meric, 'Finite element and conjugate gradient methods for a nonlinear optimal heat transfer control problem, *Int. j. numer. methods eng.*, **14**, 1851–1863 (1979).
26. R. T. Haftka, 'Techniques for thermal sensitivity analysis', *Int. j. numer. methods eng.*, **17**, 71–80 (1981).
27. K. Dems, 'Sensitivity in thermal problems I. Variation of material parameters within a fixed domain', *J. Thermal Stresses*, **9**, 303–324 (1986).
28. K. Dems, 'Sensitivity in thermal problems II. Structural shape variation', *J. Thermal Stress*, **10**, 1–16 (1986).
29. R. A. Meric, 'Shape design sensitivity analysis for nonlinear anisotropic heat conducting solids and shape optimization by the BEM, *Int. j. numer. methods eng.*, **26**, 109–120 (1988).
30. D. A. Tortorelli and R. B. Haber, 'First order design sensitivities for transient conduction problems by an adjoint method', *Int. j. numer. methods eng.*, **28**, 733–752 (1989).
31. D. A. Tortorelli, R. B. Haber, and S. C. Y. Lu, 'Design sensitivity analysis for nonlinear thermal systems', *Comput. Methods Appl. Mech. Eng.*, **77**, 61–77 (1989).
32. D. A. Tortorelli, M. M. Tiller and J. A. Dantzig, 'Optimal design of advanced parabolic systems—Part I. Fixed spatial domain with applications to process optimization', *Comput. Methods Appl. Mech. Eng.*, **113**, 141–155 (1994).
33. D. A. Tortorelli, J. A. Tomasko, T. E. Morthland, and J. A. Dantzig, 'Optimal design of parabolic systems—Part II. Variable spatial domain with applications to casting optimization', *Comput. Methods Appl. Mech. Eng.*, **113**, 157–172 (1994).
34. D. A. Tortorelli, R. B. Haber, and S. C. Y. Lu, 'Design sensitivity analysis for nonlinear transient thermal systems', *Comput. Methods Appl. Mech. Eng.*, **75**, 61–78 (1990).
35. K. Dems and Z. Mroz, 'Variational approach to sensitivity analysis in thermoelasticity', *J. Thermal Stress*, **10**, 283–306 (1987).
36. D. A. Tortorelli, G. Subramani, S. C. Y. Lu and R. B. Haber, 'Sensitivity analysis for coupled thermoelastic systems, *Int. J. Solids Struct.*, **27**, 1477– 1497 (1991).
37. R. J. Yang, 'Shape design sensitivity analysis of thermoelasticity problems', *Comput. Methods Appl. Mech. Eng.*, **102**, 41–60 (1993).
38. R. A. Meric, 'Sensitivity analysis of functionals with respect to shape for dynamically loaded nonlocal thermoelastic solids', *Int. J. Eng. Sci.*, **26**, 703–711 (1988).
39. D. A. Tortorelli, R. B. Haber and S. C. Y. Lu, 'Adjoint sensitivity analysis for nonlinear dynamic thermoelastic systems', *AIAA J.*, **29**, 253–263 (1991).

40. D. A. Tortorelli, 'Design sensitivity analysis for coupled systems and their application to concurrent engineering', in *NATO-ARMY-NASA Advanced Study Institute for Concurrent Engineering Tools and Technologies for Mechanical System Design*, Iowa City, IA, 1992.
41. R. Gunnert, *Residual Welding Stresses*, Almqvist and Wiksell, Stockholm, 1955.
42. J. F. Lancaster, *The Metallurgy of Welding Brazing and Soldering*, Modern Metallurgical Texts, George Allen and Unwin LTD, Great Britain, 1965.
43. H. Hibbitt and P. V. Marcal, 'A numerical, thermo-mechanical model for the welding and subsequent loading of a fabricated structure', *Comput. struct.*, **3**, 1145–1174 (1973).
44. B. A. B. Andersson, 'Thermal stress in a submerged-arc welded joint considering phase transformations', *Trans. ASME*, **100**, 356–362 (1978).
45. E. F. Rybicki, D. W. Schmueser, R. B. Stonesifer, J. J. Groom, and H. W. Mishler,'A finite-element model for residual stresses and deflections in Girth–Butt Welded pipes', *J. Pressure Vessel Technol*, **100**, 256–262 (1978).
46. E. F. Rybicki and R. B. Stonesifer, 'Computation of residual stresses due to multipass welds in piping systems', *J. Pressure Vessel Technol.*, **101**, 149–154 (1979).
47. K. Masubuchi, 'Models of stresses and deformation due to welding—A review', in H. D. Brody and D. Apelian, (eds.)., *Modeling of Casting and Welding Processes*, Rindge, NH, The Metallurgical Society of AIME, 1980, pp. 245–257.
48. J. H. Argyris, J. Szimmat, and K. J. Willam, 'Computational aspect of welding stress analysis', *Comput. Methods Appl. Mech. Eng.*, **33**, 635–666 (1982).
49. J. Goldak, A. Chakravarti, and M. Bibby, 'A new finite element model for welding heat sources', *Metal. Trans. B*, **15B**, 299–305 (1984).
50. J. Goldak and M. Bibby, 'Computational thermal analysis of welds: current status and future directions', in A. F. Giamei and G. J. Abbaschian, (eds.),| *Modeling of Casting and Weldin Processes IV*, The Minerals and Materials Society, Palm Coast, FL, 1988, pp. 153–166.
51. P. Tekriwal and J. Mazumder, 'Finite element analysis of three-dimensional transient heat transfer in GMA Welding', *AWS Welding J. Res.* Suppl., **67**, 150s–156s (1988).
52. J. Goldak M. Gu and E. Hughes, 'Steady state thermal analysis of welds with filler metal addition', *Can. Metal. Quart.*, **32**, 49–55 (1993).
53. A. P. Chakravati, L. M. Malik and J. A. Goldak, 'Prediction of distortion and residual stresses in panel welds', in *Computer modelling of Fabrication Processess and Constitutive Behaviour of Metals*, Ottawa, Ontario, 1986, pp. 547–561.
54. P. Tekriwal, 'Three-dimensional transient thermo-elasto-plastic modeling of gas metal arc welding using the finite element method', *Ph.D. thesis*, The University of Illinois at Urbana-Champaign, Department of Mechanical and Industral Engineering, Urbana, IL, 1989.
55. A. S. Oddy, J. A. Goldak and J. M. J. McDill, 'Numerical analysis of transformation plasticity in 3D finite element analysis of welds', *Eur. J. Mech. A/Solids*, **9**, 253–263 (1990).
56. S. E. Chidiac, D. S. Wilkinson and F. A. Mirza, 'Finite element modeling of transient heat transfer and microstructural evolution in welds. Part II. Modeling of grain growth in austenitic stainless steels', *Metal. Trans. B*, **23B**, 841–845 (1992).
57. S. Das, G. Upadhya, U. Chandra, M. J. Kleinosky and M. L. Tims, 'Finite element modeling of a single-pass GMA weldment, in T. S. Piwonka, V. Voller and L. Katgerman, (eds.), *Modeling of Casting, Welding and Advanced Solidification Processes VI*, Palm Coast, FL, The Minerals and Materials Society, 1993, pp. 593–600.
58. A. Sluzalec, 'Shape optimization of weld surface', *Int. J. Solids Struct.*, **25**, 23–31 (1989).
59. K. J. Bathe, *Finite Element Procedures in Engineering Analysis*, Prentice-Hall, Englewood Cliffs, N.J., 1982.
60. D. R. J. Owen and E. Hinton, *Finite Elements in Plasticity Theory and Practice*, Pineridge Press, Swansea, 1980.
61. Pauli Pedersen, 'A note on plasticity theory in matrix notation', *Commun. appl. numer. methods.* **3**, 541–546 (1987).
62. W. F. Chen and D. J. Han, *Plasticity for Structural Engineers*, Springer, New York, 1988.
63. J. Lubliner, *Plasticity Theory*, Macmillan, New York, 1990.
64. G. A. Maugin, *The Thermomechanics of Plasticity and Fracture*, Cambridge University Press, New York, 1992.
65. H. J. Braudel, M. Abouaf, and J. L. Chenot, 'An implicit and incremental formulation for the solution of elastoplastic problems by the finite element method', *Comput. Struct.*, **22**, 801–814 (1986).
66. PDA Engineering, *Patran Plus User's Manuals Vols I and II*, Software Products Division, Costa Mesa, CA, 1990.
67. PDA Engineering, *Patran Command Language Guide*, Software Products Division, Costa Mesa, CA, 1990.
68. J. Wray, 'Mechanical, physical and thermal data for modeling the solidification processing of steels', in H. D. Brody and D. Apelian, (eds.), *Modeling of Casting and Welding Processes*, Rindge, NH, The Metallurgical Society of AIME, 1980, pp. 245–257.
69. The British Iron and Steel Research Association, (eds.), *Physical Constants of Some Commercial Steels at Elevated Temperatures*, Butterworths Scientific Publications, London, 1953.
70. L. O. Raymond and J. Chipman, 'Thermodynamic Functions of Iron,' *Trans. Metal. Soc. AIME*, **239**, 630–633 (1967).
71. M. S. Engelman, *FIDAP Theoretical Manual*, Fluid Dynamics International, Evanston, IL, 1987.
72. R. T. Haftka, *Elements of Structural Optimization*, 3rd edn., Kluwer, Boston, 1991.
73. R. Michel, 'Elastic constants and coefficients of thermal expansion of piping materials proposed for 1954 code for pressure piping'; *Trans. ASME*, **77**, 151–159 (1955).

74. H. Mizukami, K. Mizukami and Y. Miyashita, Mechanical properties of continously cast steel at high temperatures, in *Tetsu-to-Hagane (Iron and Steel)*, Vol. **63,** 1977–S562, pp. 46 (in Japanese).
75. W. H. Hill, K. D. Shimmin and B. A. Wilcox, Elevated–temperature dynamic moduli and metallic materials, in *proc. ASTM*, Vol. 61, 1961, pp. 890–906.
76. C. J. Smithells, ed., *Metals Reference Book*, 5th edn., Butterworths, London, 1976.
77. VMA Engineering. *DOT User's Manual, Version 3.00*, Vanderplaats, Miura and Associates, Goleta, CA, 1992.